JGR Atmospheres

Key Points:
- The 3D tomographic water vapor model allows detailed monitoring of water vapor change during three super typhoon events
- Precipitable water vapor (PWV) in the lower troposphere (0–1.6 km) has almost no change during the whole life cycle of super typhoons
- PWV temporal and spatial increase rates in layers (1.6–8.5 km) are about 12.710 to 24.272 mm/day and about 0.031 to 0.037 mm/km, respectively

Observing Water Vapor Variability During Three Super Typhoon Events in Hong Kong Based on GPS Water Vapor Tomographic Modeling Technique

Mingchen Zhu[1,2,3,4], Zhizhao Liu[1,2] (iD), and Wusheng Hu[3]

[1]Department of Surveying and Geo-informatics, Hong Kong Polytechnic University, Kowloon, Hong Kong, [2]Research Institute for Sustainable Urban Development, Hong Kong Polytechnic University, Kowloon, Hong Kong, [3]School of Transportation, Southeast University, Nanjing, China, [4]School of Civil Engineering and Architecture, Tongling University, Tongling, China

Abstract This paper for the first time numerically characterizes the water vapor spatial and temporal variation during the life cycle of super typhoons, using the 3D tomographic water vapor modeling method. Global Positioning System (GPS) data sets collected in Hong Kong were used to reconstruct the water vapor density field with a temporal resolution of 30 min during three super typhoon events in 2013 and 2014. The spatiotemporal variabilities of water vapor at five altitude layers (<0.8, 0.8–1.6, 1.6–3.0, 3.0–5.2, and 5.2–8.5 km) were examined. It was found that in the lower troposphere (<1.6 km), the precipitable water vapor (PWV) had only minor fluctuation during typhoon events. But significant PWV increase was observed at altitude above 1.6 km, and PWV kept increasing with the altitude, leading to the increase of the total water vapor. Hong Kong's PWV was observed to increase as the typhoons were about 795 to 821 km away from Hong Kong. The PWV spatial (distance) increase rate was 0.031–0.037 mm/km in the upper layers (1.6–8.5 km) and temporal increase rate was 12.710–24.272 mm/day in the upper layers (1.6–8.5 km). The typhoons had the largest impact on the PWV variation in the top layer (layer 5, 5.2–8.5 km). Prior to typhoon impact, PWV in layer 5 accounts for only 12.77% to 13.68% in the upper layers (1.6–8.5 km). With the typhoon impact, the PWV in layer 5 accounts for 21.28% to 26.38%. This work has demonstrated the potential to use water vapor tomographic technique to study water vapor evolution during super typhoons.

1. Introduction

Water vapor accounts for only a very small portion in the whole atmosphere. However, it is one of the meteorological factors that are most difficult to be precisely parameterized (Rocken et al., 1997). Water vapor is also one kind of greenhouse gases (GHGs), contributing about 60% GHG effects to climate change (Wagner et al., 2006). The phase change of water vapor absorbs or releases a large amount of heat causing severe weather phenomena such as typhoon events. The IPCC's first and second assessment reports for 1990 to 2005 suggested that the global average temperature will increase by about 0.3°C and 0.15°C per decade (Solomon et al., 2007). The temperature increase has a close relationship with intensity of typhoons (Elsner et al., 2008). Heavy squally showers triggered by typhoons can result in catastrophic casualties as well as great damages to urban infrastructure and agricultural production, especially for developed coastal regions (Jessup & DeGaetano, 2008; Kawano et al., 2008; Pilon, 2002). Therefore, monitoring water vapor is significant for improving the accuracy of extreme weather forecast and studying the greenhouse effect (Emanuel et al., 1995; Weckwerth et al., 2004).

Currently, many methods have been used for water vapor measurement including radiosonde, water vapor radiometer (WVR), and satellite remote (Baker et al., 2001; Bevis et al., 1994). Bevis et al. (1992) first suggested the use of Global Positioning System (GPS) for sensing atmospheric water vapor. Ground-based GPS has gradually become one of the most important means for water vapor measurement due to its high accuracy, all-weather capability, high spatial-temporal resolution, and cost effectiveness. To determine the vertical distribution of water vapor with high temporal resolution, GPS tomographic technique has been developed (Flores et al., 2000). Based on certain numbers of slant wet delays (SWDs) collected from a GPS network, three-dimensional (3D) regional field of atmospheric wet refractivity can be reconstructed using tomographic technique with a spatial resolution of several kilometers and a temporal resolution of tens of minutes (Champollion et al., 2005; Chen & Liu, 2014; Nilsson & Gradinarsky, 2006).

With the availability of a large number of GPS stations, GPS-derived water vapor data therefrom have been widely used in meteorology and climatology, numerical weather prediction (NWP), and severe weather analysis such as heavy rainfall, typhoon, and severe flood. Champollion et al. (2004) investigated water vapor distribution and variation during the torrential precipitation episode in southern France in September 2002. The conclusion showed that the spatiotemporal variation of water vapor and the temporal variations of wet gradients could improve the understanding of large rainfall events. Using GPS observations and the European Centre for Medium-Range Weather Forecasts (ECMWF) product, Abraha et al. (2017) revealed the spatiotemporal variations of water vapor content over Ethiopia. Yeh et al. (2018) determined the precipitable water thresholds under different rainfall strengths in Taiwan. Their results indicated that the average precipitable water vapor (PWV) thresholds were 41.8, 52.9, and 62.5 mm under the light, moderate, and heavy rainfall conditions, respectively. Zhao et al. (2018) used the increment of PWV in a short time (2–6 h) and PWV slope in a longer time (a few hours to >10 h) to forecast the precipitation events. The numerical results showed that 80–90% of precipitation events and more than 90% of heavy rain events could be forecast 2–6 h in advance of the precipitation. Using a small network of GPS stations, Van Baelen and Penide (2009) investigated the vertical variability of water vapor in the lower part of the atmosphere. Comparing two episodes of higher water vapor contents, they showed that the contrasting behaviors of different layers can reveal the possible formation of clouds before a rain. Manning et al. (2012) indicated that the dynamics of water vapor had a great impact on the formation and life cycle of severe mesoscale convective storm systems by using improved Kalman filtering algorithm and GPS tomography method. Focusing on a case study from the convective and orographically induced precipitation study in a low mountain area, Labbouz et al. (2013) used GPS tomography results showing the role of low-level water vapor accumulation and convergence as a precursor to the convective initiation. By using Hong Kong tomographic data, Chen et al. (2017) examined the variability of water vapor at five altitude layers during three heavy rainfalls. It revealed that water vapor above 3 km in altitude, though accounting for only 10–25% of the total amount of water vapor, had larger fluctuation than that below 3 km.

As a highly developed and populated city, Hong Kong is located on the coast of the South China Sea with a humid subtropical climate. It is hot and humid in summer. Thunderstorms are frequent when warm air comes from the south. Hong Kong suffers from extreme weather events such as heavy rainfalls and strong typhoons. Typhoons are common in the summer and fall, sometimes resulting in flooding, accompanied with landslides. As water vapor plays a critical role in the formation of extreme weather events, monitoring and understanding the variation of water vapor during these events are thus very important for the weather forecasting.

ERA5 is the latest climate reanalysis produced by ECMWF, providing hourly data on many atmospheric, surface, and sea-state parameters with at latitude-longitude grids (0.25° × 0.25° resolution) and atmospheric parameters on 37 pressure levels (Copernicus Climate Change Service [C3S], 2017). Its daily update is available 5 days after observation. Due to the ERA5 product's 5-day latency of daily updates and relatively low temporal resolution (1 h), it is not suitable to characterize the water vapor variation during typhoon events in real or near real time. To examine the water vapor evolution during the super typhoon, high-resolution (30 min) 3D water vapor density (WVD) field data, which are reconstructed with the tomographic technique based on GPS observations, are applied. In this study, tomographic 3D water vapor data derived from GPS observations in Hong Kong are used to study water vapor variations during three super typhoon events that occurred during 2013–2014. The structure of this paper is as follows. The SWD retrieval and water vapor tomographic 3D modeling method are introduced in section 2. Section 3 studies the water vapor variation during the life cycles of three typhoons, and the discussions were given in section 4. The conclusions are summarized in section 5.

2. Method

2.1. Retrieval of SWV From GPS Data

When GPS signals pass through the lower part of the atmosphere (troposphere), the signals experience a range delay, which is usually called tropospheric delay. This delay in the zenith direction, called zenith total delay (ZTD), is usually decomposed into two components: zenith hydrostatic delay (ZHD) and zenith wet delay (ZWD). Many Global Navigation Satellite System (GNSS) data processing software packages can be

used to accurately estimate ZTD. In this study, the Bernese software is employed to process the GPS data (Dach et al., 2015).

For a GPS satellite at a slant direction, the tropospheric delay is called slant total delay (STD), which can be modeled as a function of ZHD, ZWD, plus horizontal gradients and their mapping functions in the Bernese software, as given below.

$$\text{STD} = m_h(e)*\text{ZHD} + m_w(e)\left[\text{ZWD} + \cot(e)\left(G_W^N\cos(\alpha) + G_W^E\sin(\alpha)\right)\right] \tag{1}$$

where m_h and m_w are mapping functions for the ZHD and ZWD, respectively. The Niell mapping functions (Niell, 1996) are used in this study. G_W^N and G_W^E are the horizontal gradients of wet delay in the north and east directions, respectively, which are directly estimated in the software. The horizontal gradients show the anisotropy of the local troposphere, which cannot be ignored in accurate water vapor estimation using GPS measurements. α and e, both in unit of radian, are the azimuth and the elevation angles of a GPS station toward a given GPS satellite, respectively.

The ZHD can be precisely modeled using empirical models such as Saastamoinen (1972) model. It can be modeled as Equation 2 (Davis et al., 1985; Saastamoinen, 1972):

$$\text{ZHD} = \frac{0.0022768P_0}{f(\varphi, h)} \tag{2}$$

where P_0 is the surface pressure, which can be obtained from the NWP model of Hong Kong (Wong, 2010). The function $f(\varphi, h)$ is given by Equation 3:

$$f(\varphi, h) = 1 - 0.00266\cos(2\varphi) - 0.0028h \tag{3}$$

where φ is the geodetic latitude (in unit of radian) and h is the height above geoid in unit of kilometer.

In Equation 1, after modeling and removing the ZHD term from STD, the remaining one mainly resulting from the SWD can be expressed as Equation 4:

$$\text{SWD} = m_w(e)\left[\text{ZWD} + \cot(e)\left(G_W^N\cos(\alpha) + G_W^E\sin(\alpha)\right)\right] + R \tag{4}$$

where R, referred to as the postfit residual, results from the unmodeled errors that include the ZWD, ZHD, and other unmodeled errors in GPS observations such as the multipath noise (Hirahara, 2000; Chen & Liu, 2014). By using the method proposed by Alber et al. (2000), the zero-difference residuals can be extracted from the double-difference residuals which are outputted by the software. The addition of R is necessary because the errors are usually smaller than the formal observable uncertainty and also correlated with the wet troposphere structure (Flores et al., 2000). To reduce the impact of multipath effect, GPS observation rays with an elevation angle below 10° are eliminated. Subsequently, the SWD can be converted to slant water vapor (SWV) by using the formula proposed by Bevis et al. (1992):

$$\text{SWV} = \frac{10^5}{(k_3/T_m + k'_2) \cdot R_v} \cdot \text{SWD} \tag{5}$$

where $k_3 = 3.776 \times 10^5$ k^2/hPa, $k'_2 = 16.52$ k/hPa, and $R_v = 461.495$ J/K/kg are the specific gas constants for water vapor. T_m is the weighted mean temperature, which can be calculated from surface temperature (Kelvin), which is derived from NWP model of Hong Kong, after the formula proposed by Chen et al. (2007).

2.2. Reconstruction of Wet Refractivity Field Using Tomographic Technique

The first task in GPS tomography is to discretize the troposphere over the Hong Kong region into a number of voxels. In this study, the voxel discretization refers to the method in Chen and Liu (2014), which consists of four steps: (1) setting the height of the top boundary to 8.5 km; (2) determining the optimization horizontal boundary; (3) optimizing the vertical layer discretization; and (4) moving the voxel at a specified step along the longitude and latitude to determine the optimal horizontal resolutions. Assuming that the water
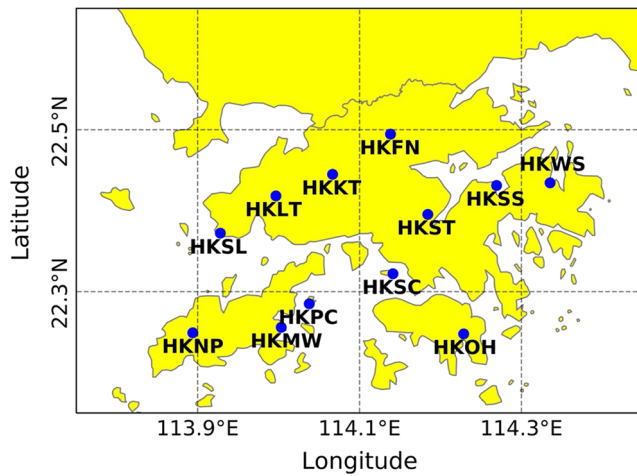
Figure 1. Locations of the 12 GPS continuously operating reference stations (blue dots) in the Hong Kong Satellite Positioning Reference Station Network (SatRef) in Hong Kong in October 2014.

vapor in each voxel is constant and evenly distributed throughout the period of time of tomographic modeling (in this study, the time is 30 min), then SWV can be approximately estimated by Equation 6 (Dong & Jin, 2018):

$$\text{SWV} = \sum_{i=1}^{n} x(i) l_i \tag{6}$$

where n is the number of voxels crossed by the specific signal ray linking ground GPS receiver and GPS satellite; x_i represents the WVD (g/m^3) of the ith voxel$_i$; and l_i refers to the intercept of the ray path within voxel$_i$. Combining a large number of rays that cross the voxels from different directions during an epoch of tomographic modeling, the WVD field can be established as Equation 7:

$$\mathbf{y} = \mathbf{A} \cdot \mathbf{x} \tag{7}$$

where $\mathbf{y}$ is the observation vector representing the SWVs; $\mathbf{A}$ is a large sparse matrix composed of the length of the ray intercepted by each voxel; and $\mathbf{x}$ is the vector of WVD in each voxel in the 3D field. In general, $\mathbf{A}$ is an ill-conditioned matrix. To resolve the ill-conditioned problem, intervoxel WVD information is used to constrain the voxels. In this study, the horizontal constraint equation imposed is based on the assumption that WVD in a voxel is a weighted mean of WVDs in the horizontally surrounding voxels. The vertical constraint information is obtained from radiosonde observations (Chen & Liu, 2014). With these constraints, the tomography equation can be described as

$$\begin{bmatrix} \mathbf{y} \\ r \\ 0 \end{bmatrix} = \begin{bmatrix} \mathbf{A} \\ \mathbf{V} \\ \mathbf{H} \end{bmatrix} \cdot \mathbf{x} \tag{8}$$

where $\mathbf{V}$ and $\mathbf{H}$ are the vertical and horizontal constraint matrices, respectively, and r is the a priori information of WVD determined by the average 3-day radiosonde observations before the tomographic experiment. As the constraints have been considered, the WVD field can be first estimated by least squares. Then, the multiplicative algebraic reconstruction technique (MART) is used to solve the equation with the initial result from the least squares to obtain a more precise solution. For more detail, see Chen and Liu (2014).

2.3. Data Collection and Processing

The ground-based GPS observations and meteorological products from the Hong Kong Satellite Positioning Reference Station Network (SatRef, https://www.geodetic.gov.hk) were used in this study. The 12 continuously operating reference stations (CORSs) with the interstation distance of 7 to 12 km are shown in Figure 1.

Based on extensive experiments (Chen & Liu, 2014), an optimal horizontal resolution of 0.08° was determined, and the tomographic voxels were separated into 15 layers from ground surface to the altitude of 8.5 km in the vertical direction. Figure 2 shows the tomographic result at 12:00 UT on 8 August 2013, which captured the details of the mean variation of WVD in the unit of g/m^3 at each layer.

According to the profile of the mean WVD, they are further sorted into five layers, which are below 0.8, 0.8 to 1.6, 1.6 to 3.0, 3.0 to 5.2, and 5.2 to 8.5 km, denoted as layers 1 to 5, respectively (see Figure 2b). In order to analyze the water vapor variation, the PWV in each layer is derived by vertically integrating the WVD along the altitude in that layer.

3. Evolution of Water Vapor During Typhoon Events

This study is focused on the water vapor variation observed during three super typhoons that hit Hong Kong in 2013–2014. The three super typhoons are Utor occurring during 9–16 August 2013, Usagi during 17–23 September 2013, and Kalmaegi during 12–27 September 2014. Typhoons are classified into four categories by the World Meteorological Organization (WMO) according to the 10-min highest average wind speed near the center of the storm, as shown in Table 1.
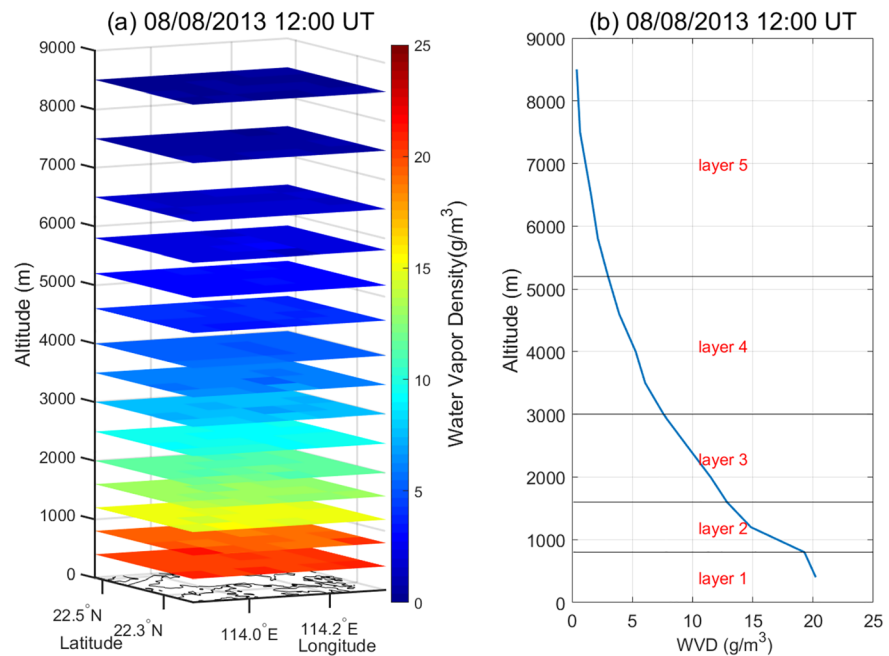
Figure 2. (a) Variation of water vapor density (WVD) at 15 altitudes over Hong Kong. (b) The average WVD profile derived from the tomographic data at 12:00 UT on 8 August 2013.

In 2009, the Hong Kong Observatory (HKO) further sorted typhoons into three different classifications: typhoon with wind speeds of 118–149 km/h; severe typhoon with wind speeds of at least 150 km/h; and super typhoon with wind speed of at least 190 km/h (HKO, 2009).

3.1. Case Study: Super Typhoon Utor (9–16 August 2013)

According to the record of HKO, tropical depression Utor was formed on 9 August 2013 about 1,350 km east of Manila, Philippines. On 11 August, Utor further enhanced to a severe typhoon. Then, its intensity increased to maximum with a central sustained wind velocity of 195 km/h on the east sea of Luzon Island, which clearly reached the level of a super typhoon. On 12 August, Utor passed Luzon and started to weaken into a severe typhoon and entered the South China Sea. On the next day, Utor turned to northwest in the south of Hong Kong. On 14 August, it approached the western coast of Guangdong Province, China, and weakened to a normal typhoon. Afterwards, Utor landed near Yangjiang and moved across the western coast of Guangdong Province, and then, it weakened to a severe tropical storm. On 15 August, Utor slowed down and moved northwards across Guangxi Province, China. On the next day, Utor finally dissipated in Guangxi Province. The track of Utor is shown in Figure 3.

Under the influence of Utor, a precipitation of more than 100 mm was recorded over parts of Hong Kong from 12 to 15 August 2013. Based on the ERA5 product, the distribution of the PWV during the period of Utor is shown in Figure 4, and the characteristic parameters for the four moments are shown in Table 2. In Table 2, the mean PWV and mean PWV increase trend, corresponding to the moments given in column 1, are calculated using the PWV 3D modeling results considering all the PWV distributed horizontally in the Hong Kong region as well as in all the layers (the same with Tables 4 and 6). Please note that the four characteristic moments in Table 2 are same as those of Figure 4.

Figure 4 and Table 2 show that PWV has the highest concentration surrounding the center of the typhoon. As Utor moved toward Hong Kong, though the maximum sustained wind speed was decreasing, both central pressure and mean PWV in the Hong Kong region were increasing. In Figure 4c, the PWV in the Hong Kong region reached its maximum when Utor was almost the closest to Hong Kong.
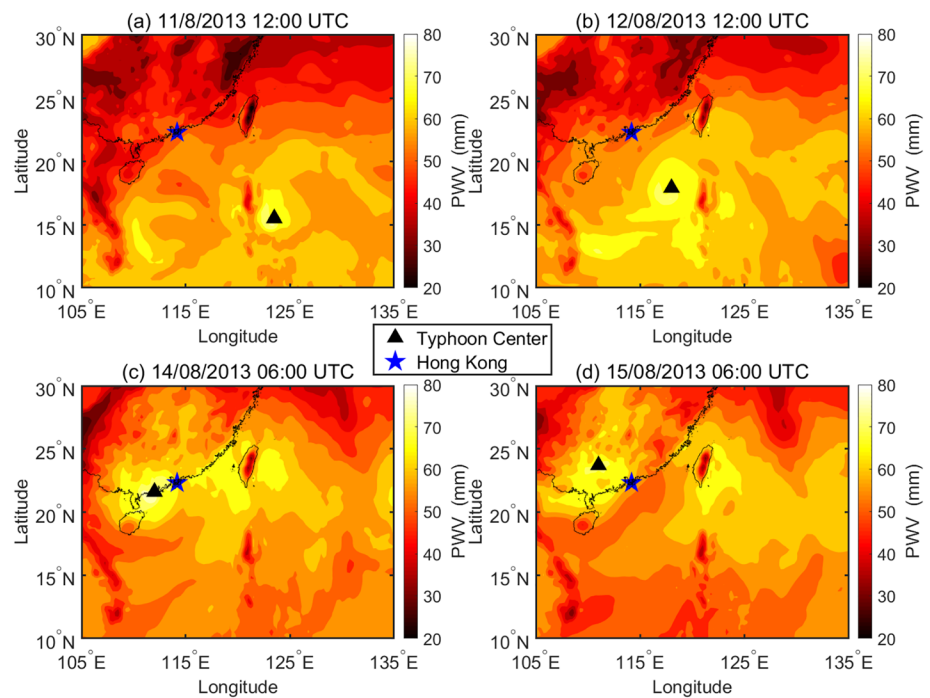
Table 1
Typhoon Classification

Categories	Wind speed near the center of the storm (km/h)
Tropical depression	41–61
Tropical storm	63–87
Severe tropical storm	88–117
Typhoon	>118
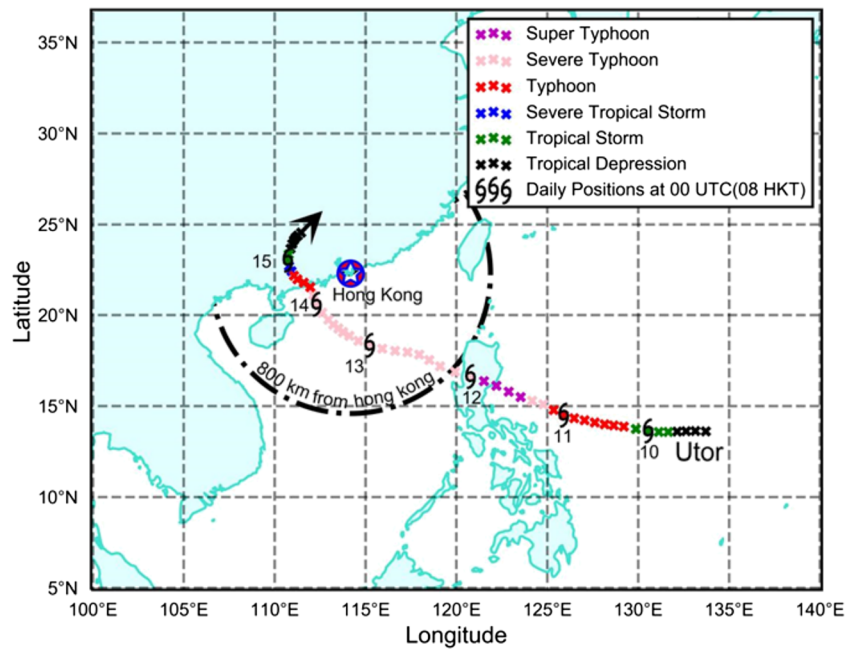
**Figure 3.** Track of Utor during the period 9–16 August 2013 (HKO, 2015a).

Figure 4. Distribution of the PWV from ERA5 product for (a) 12:00 UT on 11 August 2013 when Utor had the strongest wind speed; (b) 12:00 UT on 12 August when Utor entered the South China Sea; (c) 06:00 UT on 14 August when Utor was about the closest to Hong Kong; and (d) 06:00 UT on 15 August when Utor left Hong Kong. The black triangle refers to the typhoon center, and the blue star refers to the geographical local of Hong Kong.

Table 2
Characteristic Parameters of Utor During 11–15 August 2013

	Time (UT)	Maximum sustained wind speed (km/h)	HK mean PWV (mm)	HK mean PWV increase trend (mm/h)	Central pressure (hPa)	Distance to Hong Kong (km)
(a)	11 August 2013, 12:00	195	51.97	1.87	925	1,247.4
(b)	12 August 2013, 12:00	130	56.44	1.53	965	640.7
(c)	14 August 2013, 06:00	120	68.54	0.12	965	232.8
(d)	15 August 2013, 06:00	65	63.26	1.43	994	350.4

3.1.1. PWV Variations in Five Layers (0 to 8.5 km) During the Utor Typhoon

The tomographic PWV above the HKO synoptic station (22.30°N, 114.17°E, 60 m in altitude) was used to study the vertical variation of atmospheric water vapor during the super typhoon. The tomographic PWV for the HKO synoptic station was compared with that derived from ERA5. Figure 5a shows the evolution of tomographic PWV and Figure 5b shows PWV from tomographic modeling and ERA5 during the period of 9–18 August 2013. Figure 5a shows that the PWV of layers 1 and 2 (the lowest atmosphere) had no significant variation throughout the whole period. However, PWV of layers 3, 4, and 5 showed considerable fluctuations and the fluctuations were in correlation with the distance from the HKO synoptic station to the center of typhoon. From 9 to 11 August, layers 3 and 4 had similar variations in PWV and both fluctuated in small increments. However, layer 5 had much significant fluctuation in PWV during the same period. On 12 August, it could be seen from Figure 5a that the typhoon began to impact the PWV of layers 3, 4, and 5 at a distance of about 795 km away from Hong Kong. From 12 to 14 August, the PWV of layers 3, 4, and 5 increased rapidly when Utor was approaching Hong Kong, reaching the maximum of 16.04 mm in layer 3, 15.47 mm in layer 4, and 12.37 mm in layer 5. As Utor moved further away from Hong Kong and got weakened, the PWV of layer 5 decreased significantly, but the PWV of layers 3 and 4 still kept increasing slowly. When the typhoon left Hong Kong with a distance of 350 km, the total water vapor in Hong Kong fell to 62.32 mm, and the PWV at layer 5 was almost no longer affected by the typhoon. The PWV level in layer 3 increased to 16.18 mm.
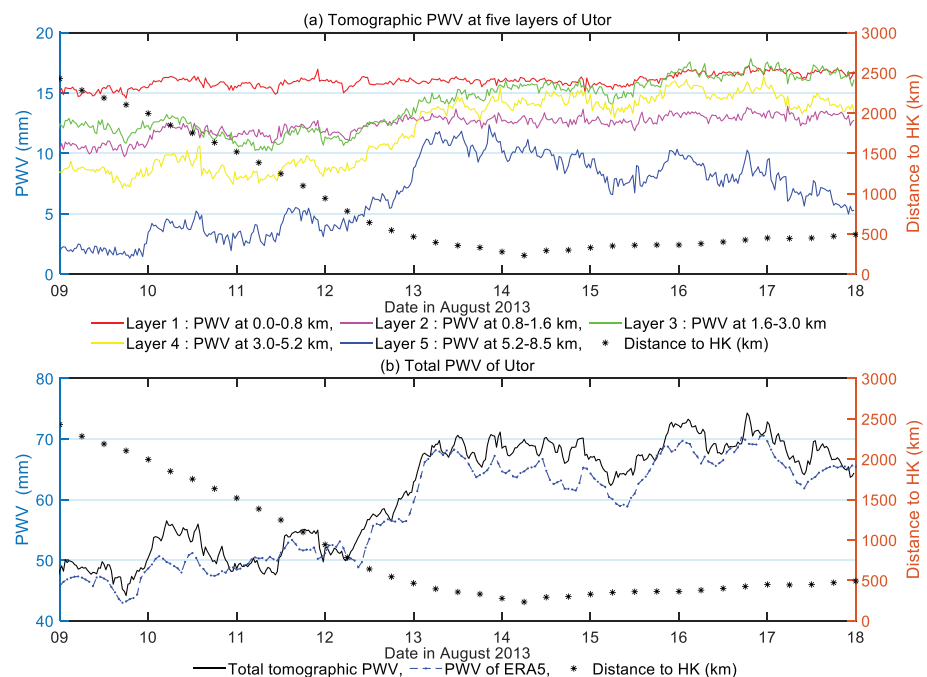
Figure 5. Evolution of (a) tomographic PWV at five layers. (b) Total PWV from tomography (black) and ERA5 (blue with triangles) during the period 9–18 August 2013 over the HKO synoptic station (22.30°N, 114.17°E, 60 m). In both (a) and (b), the black asterisks indicate the distance from the typhoon center to Hong Kong.

Table 3
PWV Statistics at the Hong Kong Synoptic Station During the Utor Typhoon From 9 to 14 August 2013 (PWV Unit: mm)

Period	Layer	Max PWV	Min PWV	Range (max–min)	Average PWV
9–11 August	3	13.22	10.22	3.00	11.82
	4	10.64	7.14	3.50	8.66
	5	5.52	1.34	4.18	3.21
12–14 August	3	16.18	10.66	5.52	14.08
	4	15.47	8.09	7.38	12.66
	5	12.37	3.11	9.26	8.63

The details are presented in Table 3. PWV statistics at the Hong Kong synoptic station during the Utor typhoon from 9 to 14 August 2013 are shown, and it can be seen from Table 3 that from 12 to 14 August, the variation range of PWV at layer 5 is 9.26 mm, which is 2.22 times of the period from 9 to 11 August. The PWV variation ranges for layers 3 and 4 are 1.84 times and 2.11 times, respectively, compared with 9 to 11 August. During 12 to 14 August, the PWV variation range at layer 5 was 1.68 times and 1.25 times of that in layers 3 and 4, respectively. During 9 to 11 August, before being affected by the typhoon, the mean PWV in layers 3, 4, and 5 accounted for 49.89%, 36.56%, and 13.55% of the three upper layers PWV, respectively. During 12 to 14 August, layers 3, 4, and 5 accounted for 39.81%, 35.79%, and 24.40% of the upper layers PWV due to effect of the typhoon. This shows that the layer 5 water vapor is more sensitive to typhoon effect.

Examining Figure 5b, it can be observed that the variation of the total PWV from tomographic model is consistent with that of the ERA5, but tomographic PWV time series has a resolution two times higher than that of ERA5. Thus, it can show more details of the variation. When the typhoon center was about 795 km to Hong Kong, the total PWV began to increase significantly, from 49.92 to 71.15 mm. To further study the variation of the mean PWV of Hong Kong in each layer, linear regression was used to quantify the variation during the PWV increase period as shown in Figure 6.

In Figure 6a, the PWV increase rates of layers 1 and 2 were −0.053 and 0.678 mm/day, respectively, during 12–14 August 2013. However, Figure 6c showed that the PWV increase rates of layers 3, 4, and 5 achieved 2.233, 3.795, and 5.642 mm/day, respectively, suggesting that the variations of PWV at the three upper layers were much more significant. Figures 6b and 6d presented the evolution of PWV with respect to the distance between the typhoon center and Hong Kong. As the typhoon center moved closer to Hong Kong, the PWV increased rapidly, particularly in the upper layers. Figure 6b showed that the PWV increase rate of the lower
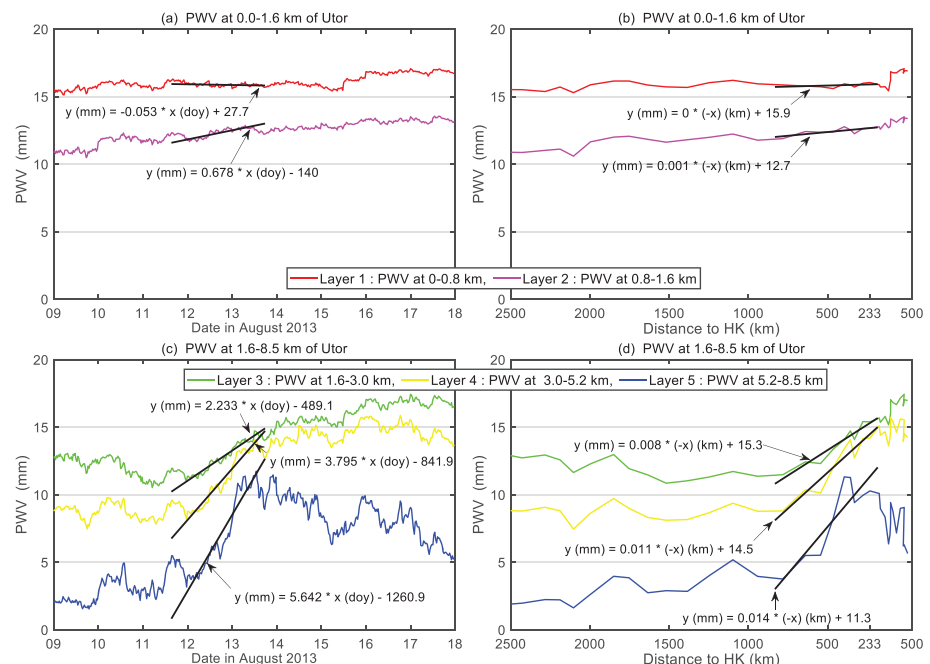
Figure 6. The linear regression of tomographic PWV with respect to day of year (doy) and distance from typhoon center to Hong Kong for the period 12–14 August 2013. (a) The linear relationship of tomographic PWV of layers 1–2 with respect to doy; (b) the linear relationship of tomographic PWV of layers 1–2 with respect to distance from typhoon center to Hong Kong; (c) the linear relationship of tomographic PWV of layers 3–5 with respect to doy; and (d) the linear relationship of tomographic PWV of layers 3–5 with respect to distance from typhoon center to Hong Kong.
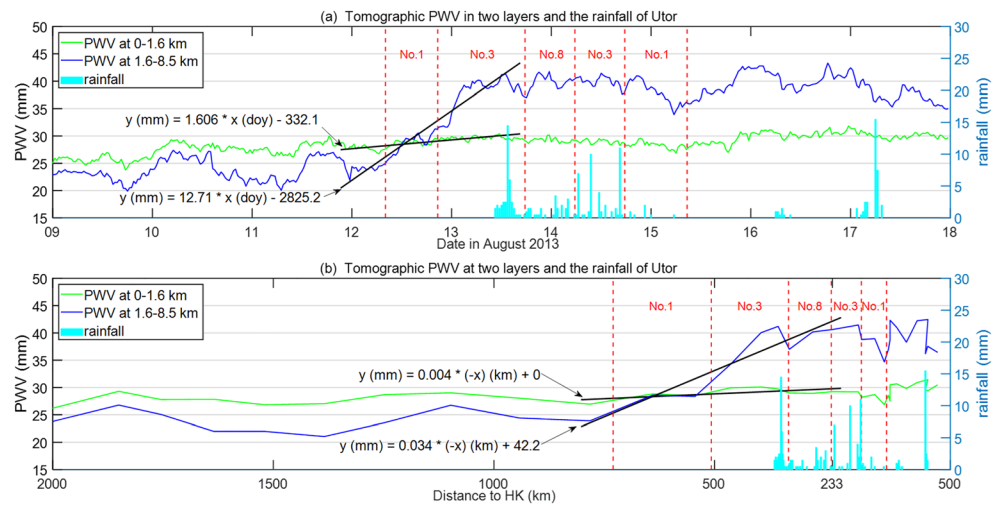
Figure 7. The linear regression of tomographic PWV with respect to day of year (doy) and distance from typhoon center to Hong Kong for the period 22:30 UT 11 August 2013 to 13:00 UT 13 August 2013. The red dotted vertical lines represent the moments when HKO issued standby signals. (a) Linear regression of tomographic PWV of the lower layers (0–1.6 km, green line) and the upper layers (1.6–8.5 km, blue line) over the HKO synoptic station with respect to day of year and (b) linear regression of tomographic PWV of the lower layers (0–1.6 km, green line) and the upper layers (1.6–8.5 km, blue line) over the HKO synoptic station with respect to the distance from typhoon center to Hong Kong. The cyan bar in (a) and (b) shows the rainfall measured by rain gauge every 30 min, with values on the right vertical axis.

two layers (layers 1 and 2) were 0.000 and 0.001 mm/km, respectively. It implied that the Utor typhoon had almost no impact on the PWV in the lower atmosphere (below 1.6 km). But the PWV increase rates of layers 3, 4, and 5 attained 0.008, 0.011, and 0.014 mm/km, respectively, as shown in Figure 6d when the Utor typhoon moved closer to Hong Kong, which were 8 to 14 times larger than bottom layers. In short, Figure 6 suggests that the Utor typhoon had larger impact on the PWV increase as altitude increases. PWV in layer 5 is the most sensitive to the effect of the typhoon. Its increase rate is the largest when the Utor typhoon approached Hong Kong and it reduced immediately when the typhoon was moving away from Hong Kong.

3.1.2. PWV Variations in Lower Layers (0–1.6 km) and Upper Layers (1.6–8.5 km) During the Utor Typhoon

As the PWV of the two bottom layers had almost no variation during the whole typhoon period, we further analyzed the PWV variation by collectively evaluating the two lower layers and the three upper layers, as shown in Figure 7. Figure 7 shows the evolution of the PWV at lower layers (0–1.6 km) and upper layers (1.6–8.5 km) over the HKO synoptic station. The standby signal no. 1 was issued at 8:05 UT on 12 August 2013, when Utor was about 710 km southeast of Hong Kong, and the total PWV over the HKO synoptic station was 52.59 mm. The higher level of signal no. 3 was issued at 20:40 UT on 12 August 2013 with a central wind speed of about 130 km/h. The total PWV was 60.74 mm at that time. As Utor continued to move northwest, it showed a greater impact on Hong Kong, and signal no. 8 was issued when Utor was about 310 km to the south-southwest of Hong Kong. Meanwhile, the total PWV increased to 66.22 mm.

Figure 7a shows that from 22:30 UT 11 August 2013 (immediately before the issuance of no. 1 signal) to 13:00 UT 13 August 2013 (immediately before the issuance of no. 8 signal), the PWV had a temporal increase rate of 1.606 mm/day in the lower layers. But the PWV increase rate of the upper layers was dramatically higher, 12.710 mm/day during the same period, which was 7.9 times of the rate of the lower layers. In terms of the PWV spatial increase rate, Figure 7b shows that the lower layers (0–1.6 km) PWV had a very small 0.004 mm/km spatial increase rate when
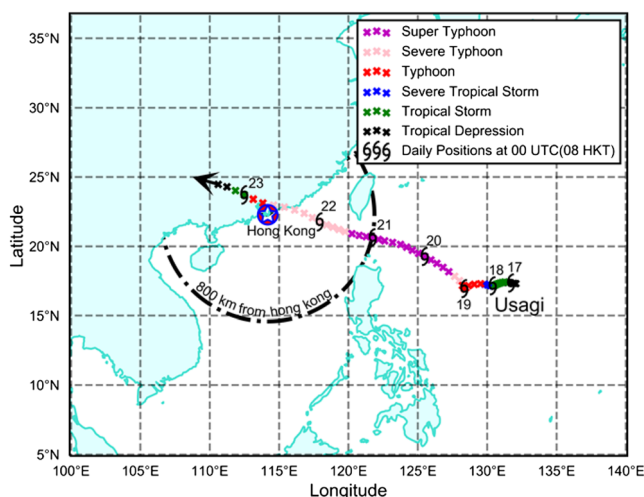
Figure 8. Track of Usagi typhoon during the period of 17–23 September 2013 (HKO, 2015a).
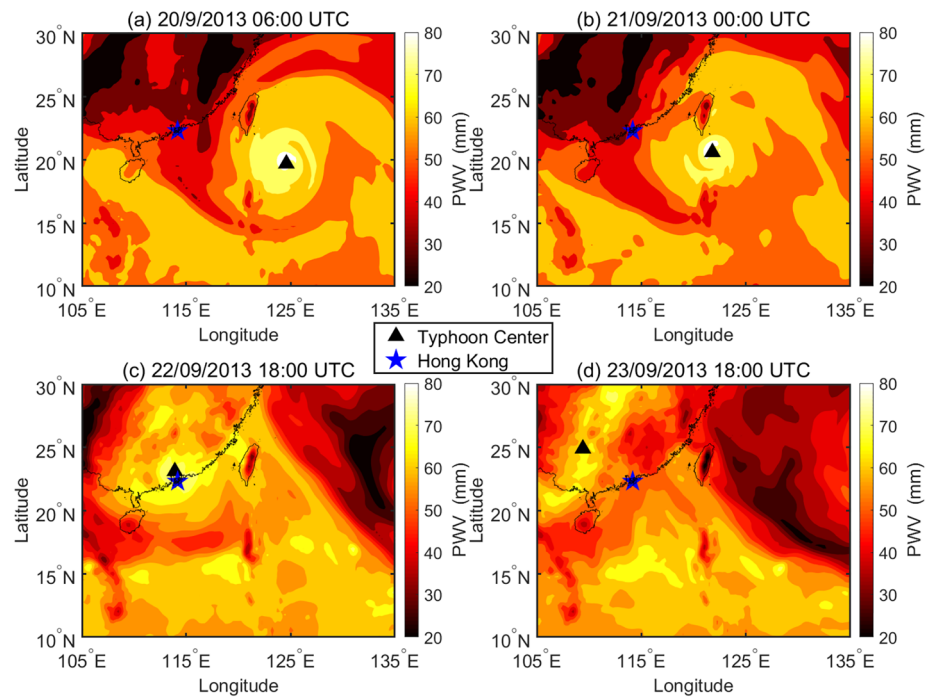
Figure 9. Contour map of PWV of 2013 typhoon Usagi at different times: (a) 06:00 UT on 20 September; (b) 00:00 UT on 21 September; (c) 18:00 UT on 22 September; and (d) 18:00 UT on 23 September.

the typhoon moved close to Hong Kong from a distance of about 710 km to a distance of 230 km. However, the PWV in the upper layers increased rapidly at a rate of 0.034 mm/km over the same course of tropical cyclone propagation, which was 8.5 times of the spatial increase rate of the lower layers.

Figure 7a shows that the PWV of the upper layers slumped after the heavy rain, immediately before the HKO's issuance of no. 8 signal (the third red dotted vertical line). The PWV then increased again rapidly under the influence of the typhoon. It can be summarized that the standby signal warning and the PWV evolution showed good consistency. The rainfall was one of the reasons for the fluctuation of the upper PWV.

3.2. Case Study: Super Typhoon Usagi (17–23 September 2013)

Usagi was the next typhoon after the Utor triggering the issuance of no. 8 gale or storm signal in Hong Kong in 2013. It was also the most violent typhoon affecting Hong Kong in that year. Figure 8 shows the track of Usagi during the typhoon period.

After forming as a tropical depression over the western North Pacific on 17 September 2013, Usagi moved westwards and intensified into a tropical storm and further strengthened into a typhoon. On 19 September 2013, Usagi reached its peak intensity with an estimated sustained wind speed of 205 km/h near its center on the next day. Figure 9a shows the impact of Usagi on PWV at the time 06:00 UT 20 September 2013. At 00:00 UT 21 September, the typhoon started to affect the water vapor in Hong Kong (see Figure 9b). Usagi entered the South China Sea and weakened into a severe typhoon. The PWV in the Hong Kong region

Table 4
Details of Usagi at the Four Stages Shown in Figure 9

	Time (UT)	Maximum sustained wind speed (km/h)	HK mean PWV (mm)	HK mean PWV increase trend (mm/h)	Central pressure (hPa)	Distance to Hong Kong (km)
(a)	20 September 2013, 06:00	203.7	49.20	−0.89	910	1,130.3
(b)	21 September 2013, 00:00	185.2	43.37	−0.21	920	821.4
(c)	22 September 2013, 18:00	92.6	71.18	1.56	975	83.9
(d)	23 September 2013, 18:00	—	56.63	−0.05	1,000	555.6
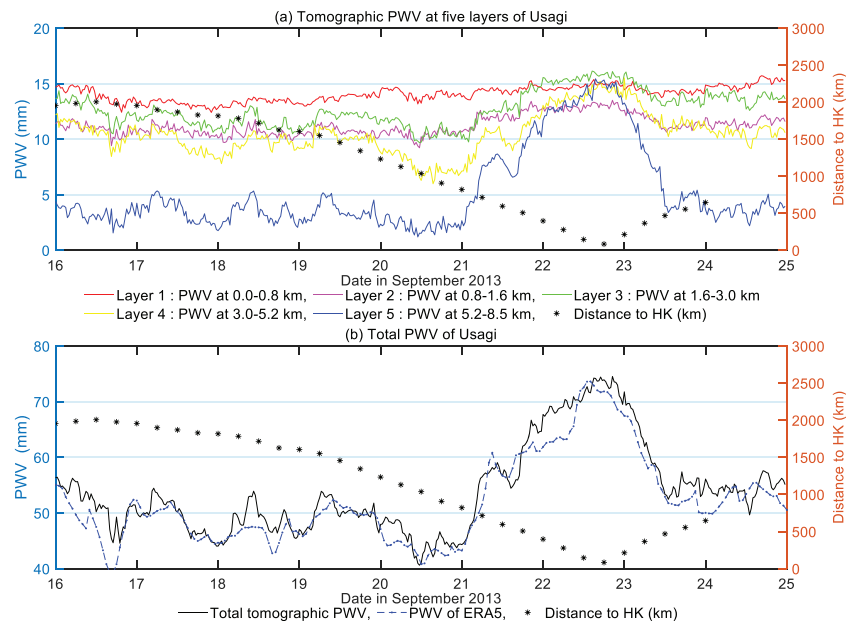
Figure 10. Same as Figure 5, but for the typhoon Usagi and for the period from 00:00 UT on 16 September 2013 to 24:00 UT on 24 September 2013.

reached its peak at the time of 16:00 UT on 22 September when Usagi was about 80 km away. Figure 9c shows the PWV affected by Usagi at the time 18:00 UT on 22 September. It can be observed from Figure 9d that after the passage of Usagi, the PWV in the Hong Kong region decreased significantly. Table 4 shows the detailed information of Usagi at four specific stages.

3.2.1. PWV Variations in Five Layers (0 to 8.5 km) During the Usagi Typhoon

The PWV variation showed a similar trend with typhoon Utor, as shown in Figure 10a. Starting from 16 September 2013, the PWV of layers 3 to 4 had the similar trend of fluctuations, followed by a visible declination beginning on 19 September. Since 21 September, the PWV of layers 3 to 5 increased rapidly. When Usagi was nearest Hong Kong, the PWV reached peak values of 16.15, 15.53, and 15.45 mm at layers 3, 4, and 5, respectively. As the typhoon moved away and weakened, the PWV of layer 5 rapidly dropped to 3.40 mm within 22 h. However, the PWV of layers 3 and 4 maintained at a high value after a slight decrease, which shows again that layer 5 is more sensitive to the effect of typhoon. In Figure 10b, the PWV derived from ERA5 data matched well with the tomographic PWV results.
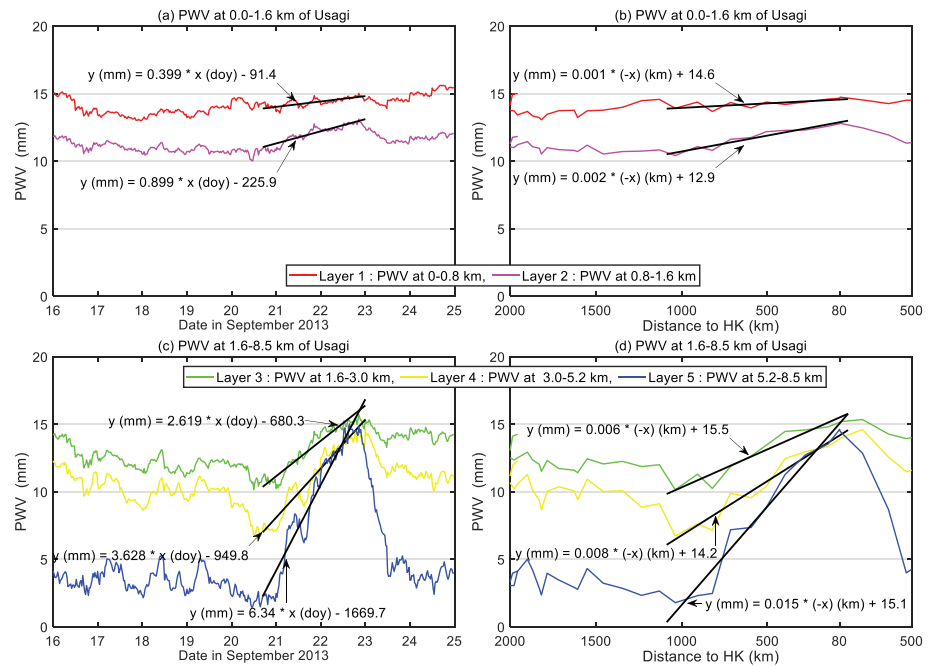
As Usagi approached Hong Kong from about 820 km away, the total PWV in Hong Kong started to rise rapidly from 44.32 to 74.42 mm when the typhoon had the shortest distance to Hong Kong. After that, the PWV dropped down to 52.46 mm as Usagi moved from Hong Kong to a distance about 483 km away.

Table 5 shows the numerical details of the PWV variations in the two periods. When affected by the typhoon, the range of PWV variation in layer 5 reached 13.24 mm, which is 2.08 times and 1.56 times of that in layers 3 and 4, respectively. The contribution of PWV of layer 5 in the three upper layers rose from 12.77% to 26.38% when comparing with the two periods. This further shows that the typhoon has the most significant impact on layer 5.

To quantitatively characterize the PWV increase, linear regression was performed for the PWV increase period in the five layers, as shown in Figure 11. Figures 11a and 11b show that the temporal and spatial rates of the PWV were very flat in both layers 1 and 2. In Figure 11c, the PWV increased steeply and the PWV increase rate in layers 3, 4, and 5 grew to 2.619, 3.628, and 6.340 mm/day, respectively. Figure 11d shows

Table 5
PWV Statistics at the Hong Kong Synoptic Station During the Usagi Typhoon From 18 to 23 September 2013 (PWV Unit: mm)

| Period	Layer	Max PWV	Min PWV	Range (max–min)	Average PWV
18–20	3	13.03	9.70	3.33	11.44
September	4	11.31	6.00	5.31	9.12
	5	5.34	1.20	4.14	3.01
21–23	3	16.15	9.77	6.38	14.08
September	4	15.53	7.04	8.49	12.04
	5	15.45	2.21	13.24	9.36

Figure 11. Same as Figure 6 but for typhoon Usagi from 16–24 September 2013.

that during 21–23 September 2013, the PWV increase rates in spatial domain of layers 3, 4, and 5 achieved 0.006, 0.008, and 0.015 mm/km, respectively. In short, it can be seen that the higher the altitude, the larger the PWV increase rate.

3.2.2. PWV Variations in Lower Layers (0–1.6 km) and Upper Layers (1.6–8.5 km) During the Usagi Typhoon

Figure 12 shows the typhoon Usagi event. As Usagi moved closer, about 160 km east-northeast of Hong Kong, signal no. 8 was issued at 10:40 UT on 22 September with the PWV increasing to 70.64 mm, and precipitation started. The heavy precipitation began at 01:00 UT on 23 September, when the PWV in the upper layers continued to decrease. After the heavy rain, the PWV in the upper layers decreased rapidly as the typhoon moved far away. Typhoon signal was canceled at 02:25 UT 23 September and the PWV was 68.94 mm, when Usagi weakened significantly inland.
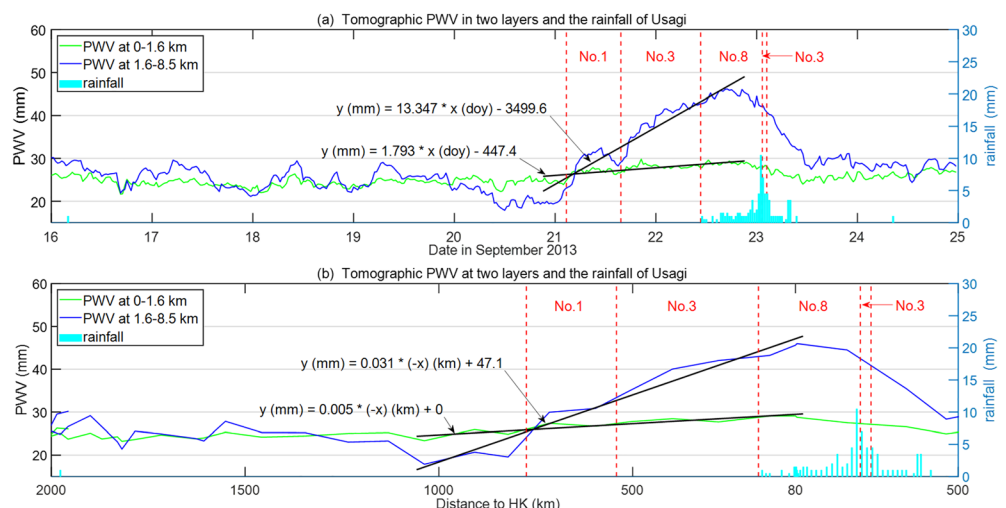
Figure 12. Same as Figure 7 but for the typhoon Usagi and for the period 00:00 UT on 16 September to 00:00 UT on 25 September 2013.
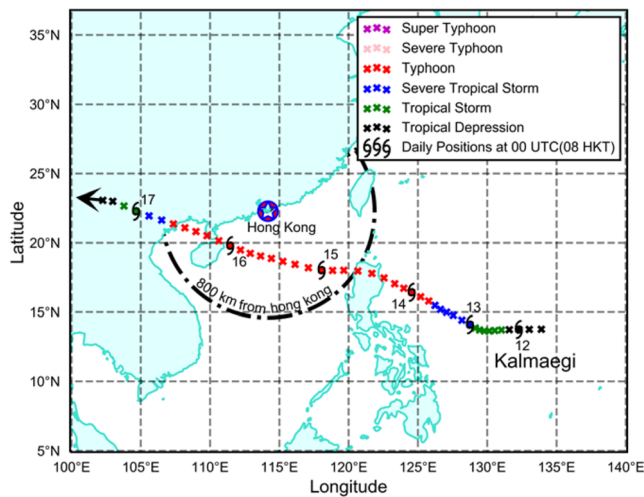
Figure 13. Track of the typhoon Kalmaegi during 12–17 September 2014 (HKO, 2015b).

Figure 12a shows that from the end of 20 September (immediately before the issuance of no. 1 signal) to the end of 23 September (soon after the issuance of no. 8 signal), the PWV had a temporal increase rate of 13.347 mm/day in the upper layers (1.6–8.5 km), which was 7.4 times of that of the lower layers. Its magnitude was very close to that of the Utor typhoon, 12.710 mm/day. In terms of PWV spatial increase rate, Figure 12b shows that the PWV in the upper layers increased rapidly at a rate of 0.031 mm/km over the same course of tropical cyclone propagation. The increase rate of upper layers was about six times of that in the lower layers. Compared with the PWV increase rate of the Utor typhoon, the increase rate 0.031 mm/km was very similar to that of Utor at 0.034 mm/km.

3.3. Case Study: Super Typhoon Kalmaegi (12–17 September 2014)

Kalmaegi was the only typhoon triggering the issuance of signal no. 8 in Hong Kong in the year 2014 (HKO, 2015b). Starting from a tropical depression about 1,430 km east of Manila in the morning of 12 September, it moved northwestwards intensifying into a typhoon. Kalmaegi was the closest to Hong Kong at about 16:00 UT on 15 September 2014 at a distance of 370 km. Moving west-northwest, Kalmaegi reached its peak intensity then made a landfall near Wenchang, Hainan Province, China. Figure 13 shows the process of its evolution.

Figures 14a and 14b show that as Kalmaegi came closer to Hong Kong, the PWV in Hong Kong increased rapidly. When its intensity grew, the PWV in Hong Kong continued to increase, though the typhoon later moved far away from Hong Kong (see Figure 14c). As Kalmaegi moved further away from Hong Kong and weakened, the PWV decreased gradually (see Figure 14d). Table 6 also shows details of Kalmaegi at four specific hours.
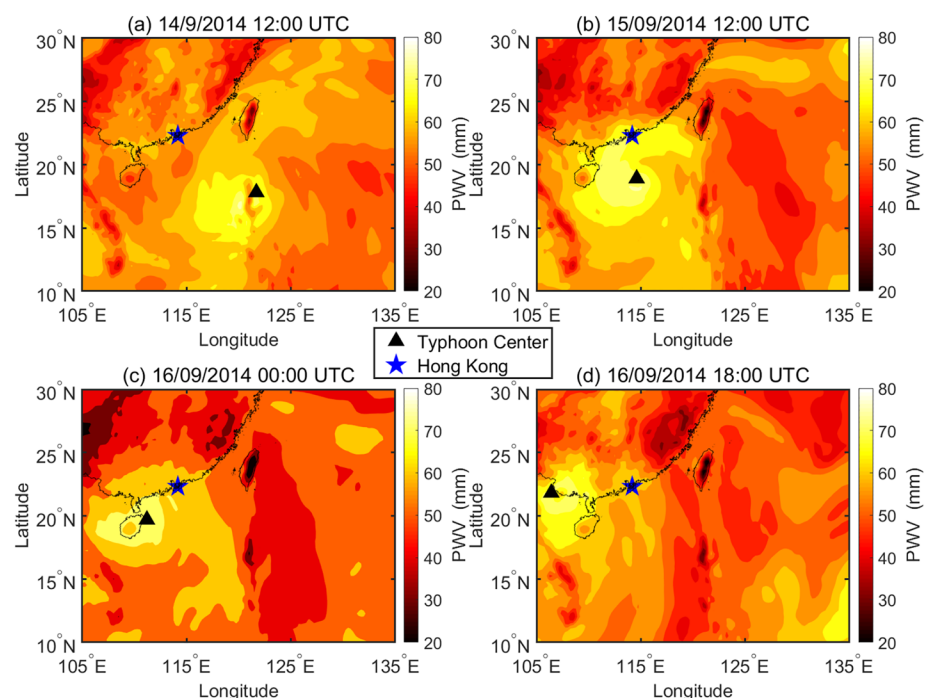
Figure 14. Same as Figure 4 but for typhoon Kalmaegi in September 2014 at (a) 12:00 UT 14 September; (b) 12:00 UT on 15 September; (c) 00:00 UT on 16 September; and (d) 18:00 UT on 16 September.

Table 6
*Details of Typhoon Kalmaegi at Four Moments in Figure 14*

	Time (UT)	Maximum sustained wind speed (km/h)	HK mean PWV (mm)	HK mean PWV increase trend (mm/h)	Central pressure (hPa)	Distance to Hong Kong (km)
(a)	14 September 2014, 12:00	120.4	62.28	2.03	970	941.6
(b)	15 September 2014, 12:00	129.6	66.80	−1.89	965	387.1
(c)	16 September 2014, 00:00	138.9	66.76	−0.95	960	421.8
(d)	16 September 2014, 18:00	101.9	63.28	−0.52	980	797.0

3.3.1. PWV Variations in Five Layers (0 to 8.5 km) During the Kalmaegi Typhoon

Figure 15 shows the evolution of PWV over the HKO synoptic station during the period 11–20 September 2014. It shows that Kalmaegi started to affect Hong Kong's PWV at a distance of 812 km. When Kalmaegi continued moving northwest, its central sustained wind speed increased and reached its peak intensity. The total PWV maintained at a high level. As it moved inland and got weakened, the PWV of the two lower layers decreased slightly, but the PWV decreased more rapidly in the three upper layers. The PWV at layer 5 continued to decrease until 1.64 mm, when Kalmaegi weakened into a low pressure over 1,300 km from Hong Kong. Figure 15b indicates that the PWV derived from tomographic model and ERA5 agreed well with each other.

Table 7 shows the numerical details of the PWV variations in two periods. The mean PWV in the three upper layers increased from 30.55 to 35.48 mm, but the contribution of layer 5 increased from 13.68% to 21.28%, which showed the same pattern as Utor and Usagi. This suggests that PWV in layer 5 was the most sensitive to typhoon event.

Figures 16a and 16c show the PWV temporal increase rates in five layers. Figures 16b and 16d show the PWV spatial increase rate with respect to the distance from Kalmaegi center to Hong Kong. Clearly, the PWV at the two lower layers below 1.6 km exhibit a very small growth rate in both temporal and spatial domains. However, the growth rates become much greater for the upper layers above 1.6 km. This is consistent with the previous two typhoon cases.
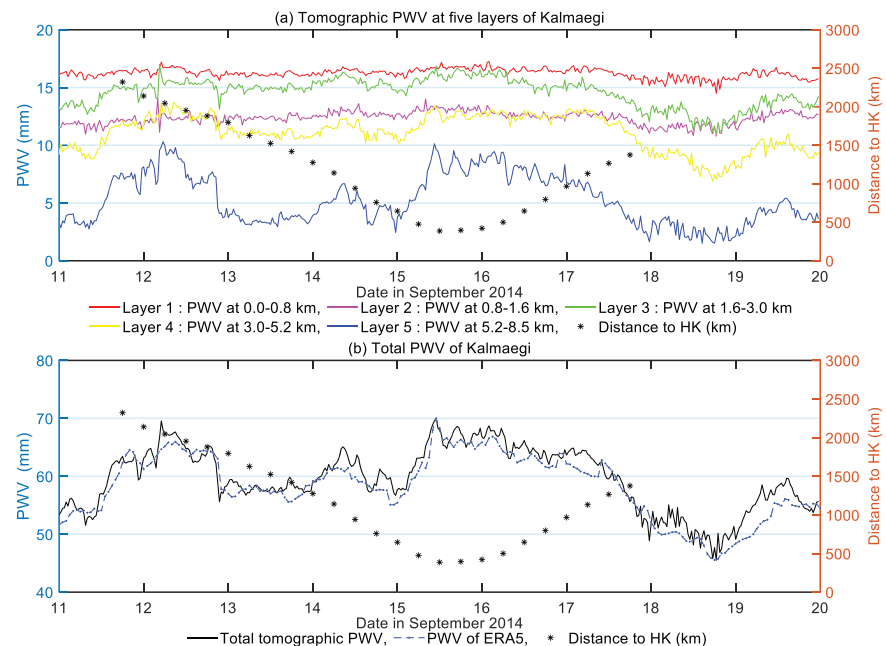
Figure 15. Same as in Figure 5 but for typhoon Kalmaegi from 00:00 UT of 11 September to 00:00 UT of 20 September 2014.

Table 7
PWV Statistics at the Hong Kong Synoptic Station During the Kalmaegi Typhoon From 13 to 16 September 2013 (PWV Unit: mm)

Period	Layer	Max PWV	Min PWV	Range (max–min)	Average PWV
13–14 September	3	16.33	14.40	1.93	15.22
	4	12.34	10.19	2.15	11.15
	5	6.68	2.45	4.23	4.18
15–16 September	3	16.85	14.23	2.62	15.65
	4	13.40	10.16	3.24	12.36
	5	10.13	3.61	6.52	7.57

3.3.2. PWV Variations in Lower Layers (0–1.6 km) and Upper Layers (1.6–8.5 km) During the Kalmaegi Typhoon

Figure 17 shows that during the typhoon Kalmaegi, signal no. 8 was issued at 14:30 UT on the same day on 15 September. The PWV of Hong Kong maintained at a high level with certain fluctuations because of some rainfalls during the signal no. 8 period then decreased rapidly to 22.43 mm at 23:30 UT on 17 September, while the PWV below 1.6 km maintained at a stable level with only minor fluctuation. The evolution process of the PWV shows a good agreement with the life cycle of Kalmaegi.

Figure 17a shows that from the end of 14 September to the middle of 15 September, the PWV had a temporal increase rate of 4.877 mm/day in the lower layers (0–1.6 km). But the rate of the upper layers (1.6–8.5 km) was dramatically higher, 24.272 mm/day, during the same period. The magnitude of the PWV increase rate in the upper layers was 1.8 times of that of Usagi and 1.9 times of that of Utor.

In terms of the PWV spatial increase rate, Figure 17b shows that the PWV in lower layers (0–1.6 km) was almost not impacted by the typhoon. However, the PWV in the upper layers (1.6–8.5 km) increased rapidly at a rate of 0.037 mm/km over the same course of typhoon propagation. This PWV spatial increase rate was almost identical to that of the Usagi (0.031 mm/km) and that of Utor (0.034 mm/km).
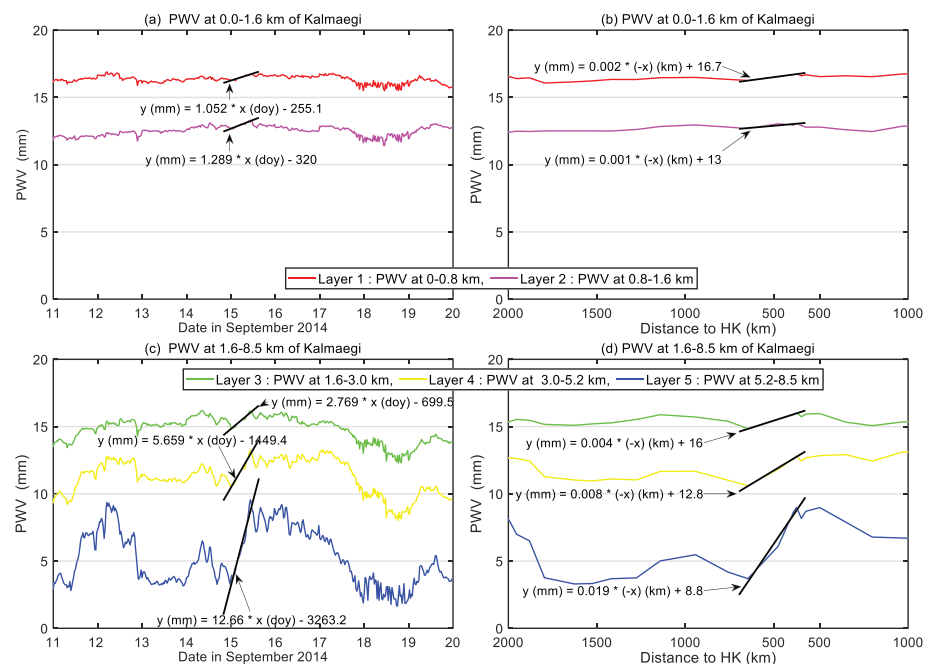
Figure 16. Same as Figure 6 but for typhoon Kalmaegi from 00:00 UT of 11 September 2014 to 00:00 UT of 20 September 2014.
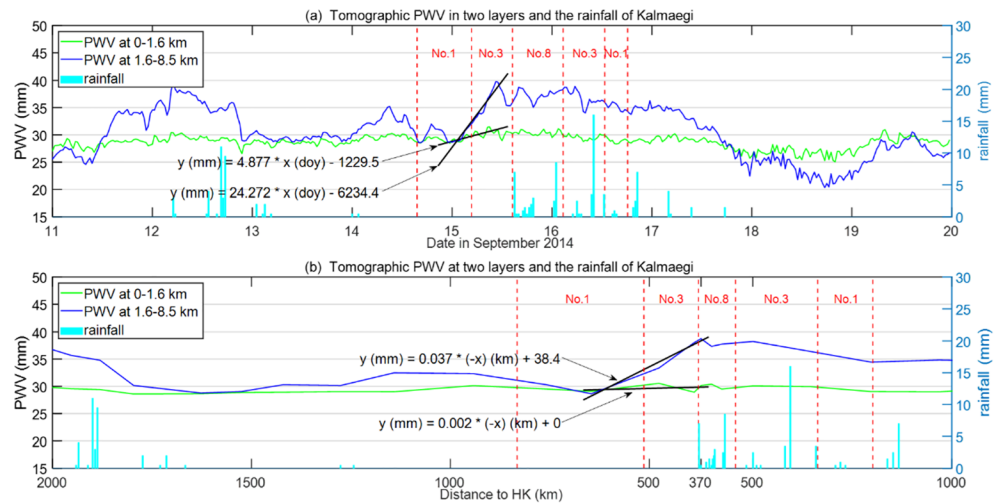
Figure 17. Same as Figure 7 but for typhoon Kalmaegi from 11 to 19 September 2014.

4. Discussion

The above analysis shows the advantage and effectiveness of the water vapor 3D tomographic model, which can illustrate clearly the PWV variation at different altitudes/layers during super typhoons. As shown in Figures 5 and 6 for the Utor typhoon, Figures 10 and 11 for the Usagi typhoon, and Figures 15 and 16 for the Kalmaegi typhoon, the PWV of layer 5 decreased the most quickly and significantly after the typhoons moved away while layers 3 and 4 basically maintained its PWV level or dropped slightly. PWV of layers 1 and 2 basically had no change.

As shown in Table 8, PWV increase is more rapid in the top layers. For the three super typhoons, both the temporal and the spatial (distance) increase rates in layer 5 were the largest range, which suggested that layer 5 is more sensitive to the effect of typhoons than other layers.

In terms of the PWV temporal increase rate, the rate of layer 5 is 106.45, 8.32, 2.53, and 1.49 times of rate of layers 1, 2, 3, and 4 in the Utor typhoon; the rate of layer 5 is 15.89, 7.05, 2.42, and 1.75 times of rate of layers 1, 2, 3, and 4 in the Usagi typhoon; and the rate of layer 5 is 12.03, 9.82, 4.57, and 2.24 times of rate of layers 1, 2, 3, and 4 in the Kalmaegi typhoon.

In terms of the PWV spatial (distance) increase rate, the rate of layer 5 is 14.00, 1.75, and 1.27 times of rate of layers 2, 3, and 4 in the Utor typhoon; the rate of layer 5 is 15.00, 7.50, 2.50, and 1.88 times of rate of layers 1, 2, 3, and 4 in the Usagi typhoon; and the rate of layer 5 is 9.50, 19.00, 4.75, and 2.38 times of rate of layers 1, 2, 3, and 4 in the Kalmaegi typhoon. Examining Figure 5, we find that the PWV in Hong Kong started to increase as the Utor typhoon was 795 km way from Hong Kong. In Figure 10, when Usagi was 821 km away from Hong Kong, it started to impact Hong Kong's PWV. Figure 15 shows that when the Kalmaegi typhoon was 819 km away from Hong Kong, the PWV started to increase.

Table 9 shows the PWV increase rates in temporal and spatial (distance) domain in lower layers (0–1.6 km) and upper layers (1.6–8.5 km) in the three typhoons. Same as Table 7, the PWV increase rates were derived

Table 8
The PWV Increase Rates in Temporal and Spatial (Distance) Domain in Layers 1–5 as the Three Typhoons Move Toward Hong Kong (Unit: mm/day for Temporal Rate and mm/km for Spatial [Distance] Rate)

	Utor		Usagi		Kalmaegi	
Layer	Temporal increase rate	Spatial increase rate	Temporal increase rate	Spatial increase rate	Temporal increase rate	Spatial increase rate
1	−0.053	0	0.399	0.001	1.052	0.002
2	0.678	0.001	0.899	0.002	1.289	0.001
3	2.233	0.008	2.619	0.006	2.769	0.004
4	3.795	0.011	3.628	0.008	5.659	0.008
5	5.642	0.014	6.340	0.015	12.660	0.019

Table 9
The PWV Increase Rates in Temporal and Spatial (Distance) Domain in Lower and Upper Layers as the Three Typhoons Move Toward Hong Kong (Unit: mm/day for Temporal Rate and mm/km for Spatial [Distance] Rate)

	Utor		Usagi		Kalmaegi	
Layer	Temporal increase rate	Spatial increase rate	Temporal increase rate	Spatial increase rate	Temporal increase rate	Spatial increase rate
Lower layers (0–1.6 km)	1.606	0.004	1.793	0.005	4.877	0.002
Upper layers (1.6–8.5 km)	12.71	0.034	13.347	0.031	24.272	0.037

from 3D tomographic water vapor modeling results. It shows that the PWV temporal increase rate in the upper layers is 7.91 times of that of lower layers in Utor typhoon; for Usagi typhoon it is 7.44 times; and it is 4.98 times in the Kalmaegi typhoon. In terms of spatial (distance) PWV increase rate, the PWV of upper layers is 8.50 times of that in lower layers in Utor typhoon; for Usagi typhoon it is 6.20 times; and it is 18.50 times in the Kalmaegi typhoon.

Water vapor plays a critical role in the development of severe weather events. During a typhoon period, strong wind brings abundant moisture from the ocean to the Hong Kong region, creating a favorable condition for squally showers. The three case studies have demonstrated the impact of typhoon on PWV variation over the Hong Kong territory. Tables 8 and 9 showed the same phenomenon: the PWV in the lower troposphere (below 1.6 km) is very stable with small PWV increase rate (temporal and spatial [distance]) and the PWV at the upper troposphere (1.6–8.5 km), however, increased significantly with much greater temporal and spatial (distance) increase rates.

In addition to the characterization of the PWV increase rate (both temporal and spatial [distance]) in different layers for the three typhoons, the 3D tomographic model has also shown the great potential to numerically quantify the impact of typhoon on PWV. Table 10 summarizes the average PWV in the upper layers (layers 1 to 3) before and after the typhoon impact. Before typhoon impact, the mean PWV of layer 5 in the upper layers accounted for only 13.55% in Utor typhoon, 12.77% in Usagi, and 13.68% in Kalmaegi. With the typhoon impact, the weight of mean PWV of layer 5 increased to 24.40% in Utor typhoon, 26.38% in Usagi, and 21.28% in Kalmaegi. The average PWV of layer 5 increased 2.69 times because of the Utor typhoon impact. For Usagi and Kalmaegi typhoons, the average PWV of layer 5 increased by 3.11 times and 1.81 times, respectively. For layer 3, the average PWV increased 1.19, 1.23, and 1.03 times due to the impact of Utor, Usagi, and Kalmaegi typhoons. For layer 4, the average PWV increased 1.46, 1.32, and 1.11 times due to the impact of Utor, Usagi, and Kalmaegi typhoons. This clearly demonstrates the advantage of the 3D tomography in depicting the detailed water vapor variation due to typhoons in different altitudes.

The 3D tomographic modeling method can clearly illustrate the PWV variation during the phase of each typhoon signal issued by the HKO. Table 11 shows that the tomographic PWV observed at the HKO synoptic station increased every time as the typhoon signal issued by the HKO escalated. In the Utor typhoon, the mean PWV increased from 57.34 to 67.48 to 69.10 mm as the signal level escalated from no. 1 to no. 3 and finally to no. 8. Compared with the no. 1 signal, the PWV level of no. 3 and no. 8 increased by 17.68% and 20.51%, respectively. In the Usagi typhoon, the mean PWV increased from 56.05 to 66.94 to 73.15 mm as the signal level escalated from no. 1 to no. 3 and finally to no. 8. Compared with the no. 1 signal, the PWV level of no. 3 and no. 8 increased by 19.43% and 30.51%, respectively. In the Utor typhoon, the mean PWV increased from 59.03, 66.15, and 67.65 mm as the signal level escalated from no. 1 to no. 3 and finally to no. 8. Compared with the no. 1 signal, the PWV level of no. 3 and no. 8 increased by 12.06% and 14.60%, respectively. This suggests that the issuance of the typhoon signals is consistent with the PWV increase trend in the typhoons.

Tables 8 to 11 present detailed information of PWV variations in different layers and with respect to different levels of typhoon signals, for all the

Table 10
Comparison of Average PWV in the Upper Layers (Layers 1 to 3) Before and After the Typhoon Impact

Period	Layer	Utor	Usagi	Kalmaegi
Before the typhoon impact	3	11.82	11.44	15.22
	4	8.66	9.12	11.15
	5	3.21	3.01	4.18
After the typhoon impact	3	14.08	14.08	15.65
	4	12.66	12.04	12.36
	5	8.63	9.36	7.57

Note. For more details, see Tables 3, 5, and 7.

Table 11
PWV Observed at the Hong Kong Observatory Synoptic Station at Different Periods in Three Super Typhoons

Time		PWV of Utor (mm)	PWV of Usagi (mm)	PWV of Kalmaegi (mm)
Standby	Start	52.59	47.92	57.90
signal no. 1	Mean	57.34	56.05	59.03
	End	60.74	55.88	61.71
Standby	Start	60.74	55.88	61.71
signal no. 3	Mean	67.48	66.94	66.15
	End	66.22	70.64	66.14
Standby	Start	66.22	70.64	66.14
signal no. 8	Mean	69.10	73.15	67.65
	End	69.62	70.25	68.37

three typhoons. The increase rates of the three typhoons are basically comparable with each other, except that the ones in Kalmaegi typhoon are larger than the other two typhoons. It can be seen that mean PWV of no. 3 signal is higher than that of no. 1 by a percentage of 12.06% to 19.43%. Comparing no. 8 signal to no. 1, the mean PWV increased by 14.60% to 30.51%. Though PWV variations are different in different typhoons, the PWV increase trend and magnitude in the three typhoons, however, are basically similar. If more typhoons are studied and more data analyses are performed in the future, it is expected that we will have a better understanding of the characteristic of PWV increase under the impact of typhoons. Knowing the PWV increase characteristics under the typhoon impact will be valuable for weather forecasters to predict the heavy precipitations and other linking typhoon impacts.

5. Conclusions

This paper describes the use of GPS-based tomography technique to monitor and illustrate the vertical distribution (five layers) and variation of water vapor during the evolution process of three super typhoons between 2013 and 2014 in Hong Kong.

The PWV at five different altitudes derived from tomographic modeling is the focus of analysis. We found the following.

1. The PWV in the lower troposphere in Hong Kong (0–1.6 km in altitude) has little change during the whole process of super typhoons because the atmosphere is almost saturated. The PWV temporal increase rate in layer 1 (below 0.8 km) is −0.053 to 1.052 mm/day, and in layer 2 (0.8–1.6 km), it is 0.678 to 1.289 mm/day.

2. The PWV in the upper layers of the atmosphere (1.6–8.5 km), particularly layer 5, increased more significantly as the PWV is pushed higher by the typhoon. In layer 3 (1.6–3.0 km), the PWV temporal increase rate is 2.233 to 2.769 mm/day; in layer 4 (3.0–5.2 km), the rate is 3.795 to 5.659 mm/day; and it is 5.642 to 12.660 mm/day in layer 5. The magnitude of the PWV temporal increase rate becomes larger as altitude increases. Moreover, the variation range of the rate becomes larger too as altitude increases.

3. The PWV in each layer increases along with the approach of the typhoon to Hong Kong. Similar to the temporal increase rate, the magnitude of the PWV spatial (distance) increase rate also grows with altitude. In both layers 1 and 2, the spatial (distance) increase rate is quite small, in the range of 0 to 0.002 mm/km; in layer 3, the rate grows to 0.004 to 0.008 mm/km; and in layer 4, the rate even grows to 0.008 to 0.011 mm/km. In the top layer 5, the PWV spatial (distance) increase rate becomes 0.014 to 0.019 mm/km. If jointly considering layers 3 to 5, the PWV spatial (distance) increase rate is in the range of 0.031–0.037 mm/km as the three typhoons approached Hong Kong.

4. When the typhoons were about 795 to 821 km from Hong Kong, they started to impact Hong Kong's PWV and the PWV started to increase.

5. Owing to the impact of typhoons, the PWV in layer 5 took a larger percentage in the upper layers. The PWV of layer 5 accounts for 24.40%, 26.38%, and 21.28% in Utor, Usagi, and Kalmaegi in the upper layers. In comparison, the PWV of layer 5 accounts for just 12.77% to 13.68% in the upper layers before the impact of the three typhoons.

This study demonstrates the effectiveness of using 3D tomographic technique to monitor atmospheric PWV during typhoon events. Unlike the ERA5 products, 3D tomography can obtain 3D water vapor distribution data in real time or near real time. We have shown that the impact of typhoon events on PWV spatial and temporal variations can be observed through monitoring the PWV accumulation, saturation, and condensation.

Data Availability Statement

All of the data used in this study are to be stored for 5 years in the Hong Kong Polytechnic University (PolyU), but can also be found at https://doi.org/10.6084/m9.figshare.12526238.

References

Abraha, K. E., Lewi, E., Masson, F., Boy, J.-P., & Doubre, C. (2017). Spatial-temporal variations of water vapor content over Ethiopia: A study using GPS observations and the ECMWF model. *GPS Solutions*, *21*(1), 89–99. https://doi.org/10.1007/s10291-015-0508-7

Alber, C., Ware, R., Rocken, C., & Braun, J. (2000). Obtaining single path phase delays from GPS double differences. *Geophysical Research Letters*, *27*(17), 2661–2664. https://doi.org/10.1029/2000GL011525

Baker, H., Dodson, A., Penna, N., Higgins, M., & Offiler, D. (2001). Ground-based GPS water vapour estimation: Potential for meteorological forecasting. *Journal of Atmospheric and Solar-Terrestrial Physics*, *63*(12), 1305–1314. https://doi.org/10.1016/S1364-6826(00)00249-2

Bevis, M., Businger, S., Chiswell, S., Herring, T. A., Anthes, R. A., Rocken, C., & Ware, R. H. (1994). GPS meteorology: Mapping zenith wet delays onto precipitable water. *Journal of Applied Meteorology*, *33*(3), 379–386. https://doi.org/10.1175/1520-0450(1994)033<0379:GMMZWD>2.0.CO;2

Bevis, M., Businger, S., Herring, T. A., Rocken, C., Anthes, R. A., & Ware, R. H. (1992). GPS meteorology: Remote sensing of atmospheric water vapor using the Global Positioning System. *Journal of Geophysical Research*, *97*(D14), 15787–15,801. https://doi.org/10.1029/92JD01517

Champollion, C., Masson, F., Bouin, M.-N., Walpersdorf, A., Doerflinger, E., Bock, O., & Van Baelen, J. (2005). GPS water vapour tomography: Preliminary results from the ESCOMPTE field experiment. *Atmospheric Research*, *74*(1–4), 253–274. https://doi.org/10.1016/j.atmosres.2004.04.003

Champollion, C., Masson, F., Van Baelen, J., Walpersdorf, A., Chéry, J., & Doerflinger, E. (2004). GPS monitoring of the tropospheric water vapor distribution and variation during the 9 September 2002 torrential precipitation episode in the Cévennes (southern France). *Journal of Geophysical Research*, *109*, D24102. https://doi.org/10.1029/2004JD004897

Chen, B., & Liu, Z. (2014). Voxel-optimized regional water vapor tomography and comparison with radiosonde and numerical weather model. *Journal of Geodesy*, *88*(7), 691–703. https://doi.org/10.1007/s00190-014-0715-y

Chen, B., Liu, Z., Wong, W.-K., & Woo, W.-C. (2017). Detecting water vapor variability during heavy precipitation events in Hong Kong using the GPS tomographic technique. *Journal of Atmospheric and Oceanic Technology*, *34*(5), 1001–1019. https://doi.org/10.1175/jtech-d-16-0115.1

Chen, Y. Q., Liu, Y. X., Wang, X. Y., & Li, P. H. (2007). GPS real-time estimation of precipitable water vapor-Hong Kong experiences. *Acta Geodaetica et Cartographica Sinica*, *36*, 9–12.

Copernicus Climate Change Service (C3S) (2017): ERA5: Fifth generation of ECMWF atmospheric reanalyses of the global climate. Copernicus Climate Change Service Climate Data Store (CDS). https://cds.climate.copernicus.eu/cdsapp#!/home

Dach, R., Lutz, S., Walser, P., & Fridez, P. (Eds) (2015). *Bernese GNSS software version 5.2*, Bern, Switzerland: Bern Open Publishing, Astronomical Institute, University of Bern. https://doi.org/10.7892/boris.72297

Davis, J. L., Herring, T. A., Rogers, A. E. E., & Elgered, G. (1985). Geodesy by radio interferometry: Effects of atmospheric modeling errors on estimates of baseline length. *Radio Science*, *20*(6), 1593–1607. https://doi.org/10.1029/RS020i006p01593

Dong, Z., & Jin, S. (2018). 3-D water vapor tomography in Wuhan from GPS, BDS and GLONASS observations. *Remote Sensing*, *10*(2), 62. https://doi.org/10.3390/rs10010062

Elsner, J. B., Kossin, J. P., & Jagger, T. H. (2008). The increasing intensity of the strongest tropical cyclones. *Nature*, *455*(7209), 92–95. https://doi.org/10.1038/nature07234

Emanuel, K., Raymond, D., Betts, A., Bosart, L., Bretherton, C., Droegemeier, K., et al. (1995). Report of the first prospectus development team of the US Weather Research Program to NOAA and the NSF. *Bulletin of the American Meteorological Society*, *76*(7), 1194–1208. https://www.jstor.org/stable/26232528

Flores, A., Ruffini, G., & Rius, A. (2000). 4D tropospheric tomography using GPS slant wet delays. *Annales Geophysicae*, *18*(2), 223–234. https://doi.org/10.1007/s00585-000-0223-y

Hirahara, K. (2000). Local GPS tropospheric tomography, *Earth*. *Planets and Space*, *52*(11), 935–939. https://doi.org/10.1186/BF03352308

HKO (Hong Kong Observatory) (2009): http://www.weather.gov.hk/informtc/classc.htm

HKO (Hong Kong Observatory) (2015a). Tropical cyclones in 2013*Rep*.

HKO (Hong Kong Observatory) (2015b). Tropical cyclones in 2014*Rep*.

Jessup, S. M., & DeGaetano, A. T. (2008). A statistical comparison of the properties of flash flooding and nonflooding precipitation events in portions of New York and Pennsylvania. *Weather and Forecasting*, *23*(1), 114–130. https://doi.org/10.1175/2007WAF2006066.1

Kawano, N., Ito, O., & Sakagami, J.-I. (2008). Flash flooding resistance of rice genotypes of *Oryza sativa* L., *O. glaberrima* Steud., and interspecific hybridization progeny. *Environmental and experimental botany*, *63*(1–3), 9–18. https://doi.org/10.1016/j.envexpbot.2007.12.001

Labbouz, L., Van Baelen, J., Tridon, F., Reverdy, M., Hagen, M., Bender, M., et al. (2013). Precipitation on the lee side of the Vosges Mountains: Multi-instrumental study of one case from the COPS campaign. *Meteorologische Zeitschrift*, *22*(4), 413–432. https://doi.org/10.1127/0941-2948/2013/0413

Manning, T., Zhang, K., Rohm, W., Choy, S., & Hurter, F. (2012). Detecting severe weather in Australia using GPS tomography. *Journal of Global Positioning Systems*, *11*(1), 58–70.

Niell, A. E. (1996). Global mapping functions for the atmosphere delay at radio wavelengths. *Journal of Geophysical Research*, *101*(B2), 3,227–3,246.

Nilsson, T., & Gradinarsky, L. (2006). Water vapor tomography using GPS phase observations: Simulation results. *IEEE Transactions on Geoscience and Remote Sensing*, *44*(10), 2927–2941. https://doi.org/10.1109/TGRS.2006.877755

Pilon, P. J. (2002). Guidelines for reducing flood losses*Rep*., United Nations International Strategy for Disaster Reduction (UNISDR).

Rocken, C., Anthes, R., & Exner, M. (1997). Analysis and validation of GPS/MET data in the neutral atmosphere. *Journal of Geophysical Research*, *102*(D25), 29,849–29,866. https://doi.org/10.1029/97JD02400

Saastamoinen, J. (1972). Atmospheric correction for the troposphere and stratosphere in radio ranging satellites, *The Use of Artificial Satellites for Geodesy*, *15*, 247–251. https://doi.org/10.1029/GM015p0247

Solomon, S., Qin, D., Manning, M., Averyt, K., & Marquis, M. (2007). *Climate change 2007: The physical science basis. Contribution of Working Group I to the Fourth Assessment Report of the Intergovernmental Panel on Climate Change*, New York, NY: Cambridge University Press.

Van Baelen, J., & Penide, G. (2009). Study of water vapor vertical variability and possible cloud formation with a small network of GPS stations. *Geophysical Research Letters*, *36*, L02804. https://doi.org/10.1029/2008gl036148

Wagner, T., Beirle, S., Grzegorski, M., & Platt, U. (2006). Global trends (1996–2003) of total column precipitable water observed by Global Ozone Monitoring Experiment (GOME) on ERS-2 and their relation to near-surface temperature. *Journal of Geophysical Research*, *111*, D12102. https://doi.org/10.1029/2005JD006523

Weckwerth, T. M., Parsons, D. B., Koch, S. E., Moore, J. A., LeMone, M. A., Demoz, B. B., et al. (2004). An overview of the International H2O Project (IHOP_2002) and some preliminary highlights. *Bulletin of the American Meteorological Society*, *85*(2), 253–278. https://doi.org/10.1175/BAMS-85-2-253

Wong, W. K. (2010). *Development of operational rapid update non-hydrostatic NWP and data assimilation systems in the Hong Kong Observatory, Beppu, Japan*, Beppu, Japan: The 3rd International Workshop on Prevention and Mitigation of Meteorological Disasters in Southeast Asia. http://www.weather.gov.hk/publica/reprint/r882.pdf

Yeh, T.-K., Shin, H.-C., Wang, C.-S., Chen, C.-H., & Hong, J.-S. (2018). Determining the precipitable water vapor thresholds under different rainfall strengths in Taiwan. *Advances in Space Research*, *61*(3), 941–950.

Zhao, Q., Yao, Y., & Yao, W. (2018). GPS-based PWV for precipitation forecasting and its application to a typhoon event. *Journal of Atmospheric and Solar-Terrestrial Physics*, *167*, 124–133. https://doi.org/10.1016/j.jastp.2017.11.013